Electronic Supplementary Material (ESI) for Journal of Materials Chemistry A.

SUPPORTING INFORMATION

Engineering Surface Atomic Structure of $FeVO_4$ Nanocrystals for use as Highly Active and Stable Electrocatalysts for Oxygen Evolution

Wei Wang, Yajun Zhang, Xiaojuan Huang, and Yingpu Bi*

State Key Laboratory for Oxo Synthesis and Selective Oxidation, National Engineering Research Center for Fine Petrochemical Intermediates, Lanzhou Institute of Chemical Physics, Chinese Academy of Sciences, 730000 Lanzhou, China

E-mail: yingpubi@licp.cas.cn

Experimental Section

chemical reagents

Iron (III) nitrate hexahydrate ($FeCl_3 \cdot 6H_2O$, 99.0%), ammonium metavanadate (NH_4VO_3, 99.0%), ethanol (CH_3CH_2OH, 99.7%), nitric acid (HNO_3, 65.0-68.0%), hydrochloric acid (HCl, 37.0%), sodium hydroxide (NaOH, 96.0%) were purchased from Sinopharm Chemical Reagent Co. Ltd. RuO_2 (99.9%) was purchased from Shanghai Macklin Biochemical Co., Ltd. Deionized water (18 MV, Molecular) was used for all solution preparations.

Material preparation.

$FeVO_4$ nanobelts: A one-step hydrothermal method was used to prepare $FeVO_4$ nanobelts [1]. Typically, 4.0 mmol of $FeCl_3 \cdot 6H_2O$ was dissolved in 20 mL of deionized water to form a clear orange solution and 4.0 mmol of NH_4VO_3 was dissolved into another 20 mL deionized water at 80 ^oC for 5 min to enhance complete dissolution. The NH_4VO_3 solution was then added into the $FeCl_3 \cdot 6H_2O$ solution which quickly formed a yellow nanoparticle colloid. After being stirred for 30 min, the suspension was transferred into a 100 mL Teflon-lined stainless-steel autoclave, which was sealed and heated in an oven at 180 ^oC for 3 h, and then cooled to room temperature naturally. The orange precipitate was collected by centrifugation, washed with deionized water and absolute ethanol several times and finally dried at 60 ^oC for 6 h.

$FeVO_4$ nanosheets: Similar preparation procedure with nanobelts was used to prepare $FeVO_4$ nanosheets except heating at 180 ^oC for 30 min.

Electrode preparation

A measure of 5.0 mg of the as-prepared powders was dispersed in the mixture solution of 0.5 ml H_2O, 0.5 ml ethanol, 0.25 ml 2-propanol and 10.0 μl 5% Nafion (ethanol solution) by sonication for 90 min. A measure of the above suspension was drop-casted onto a Ni foam (1.0 cm × 1.0 cm), which was pre-treated with concentrated HCl solution in an ultrasound bath for 5 min and cleaned by deionized water and absolute ethanol for three time. After drying at 60 ^oC for 15 min, the prepared electrode was used as the working electrode for measurements.

Materials characterization

The morphology and size of the samples were characterized by using a field-emission scanning electron microscope (JSM-6701F, JEOL) operated at an accelerating voltage of 5 kV. Transmission electron microscopy (TEM) measurements were carried out by using a FEI Tecnai

TF20 microscope operated at 200 kV. The X-ray diffraction spectra (XRD) measurements were performed on a PANalytical X'Pert PRO instrument using Cu Ka radiation (40 kV) at a scan rate of 0.067 °/s in the 2θ range from 10° to 80°. Fourier Transform Infrared spectra were recorded from pressed KBr discs on a Nexus 870 spectrometer (FTIR, Nicolet). X-ray photoelectron spectroscopy (XPS) was performed by an ESCALAB 250Xi photoelectron spectrometer. The N_2 gas sorption isotherm was measured on a Micromeritics ASAP 2020 at 77 K. The surface area was calculated by the Brunauer-Emmett-Teller (BET) method.

The photoluminescence spectra were obtained with Edinburgh LP920 with an excitation wavelength of 350 nm. The picosecond-resolved fluorescence transient plots were carried by Fluoromax-4 spectrometer. The fluorescence decay plots were measured with an excitation leaser of 341 nm and detected at 460 nm.

Temperature-programmed reduction (TPR) experiments were carried out in AutoChem II 2920 instrument. Samples of 15 mg were pretreated in He stream (30 mL min^{-1}) at 300 °C for 1 h. After cooling down to room temperature in a He flow, the gas was switched to a 10 % H_2/Ar mixture (30 mL min^{-1}) and the temperature was increased to 900 °C at a rate of 10 °C min^{-1} while monitoring the hydrogen consumption with a MS detector.

Electrochemical Measurements

The electrochemical measurements were carried out in a glass cell with an electrochemical workstation (CH Instruments 660D) in a standard three-electrode configuration, which was composed of working electrode ($FeVO_4$ samples deposited on NF electrodes), counter electrode (Pt net, 1×1 cm^2) and reference electrode (Ag/AgCl). The electrolyte was 1.0 M KOH, and the applied potentials were converted with respect to reversible hydrogen electrode (RHE), $E_{RHE} = E_{\mathrm{Ag/AgCl}} + 0.059pH + 0.197V$, and overpotential $\eta = E_{RHE} - 1.23V$. Linear scan voltammograms (LSV) were performed from 0.2 to 1.0 V vs. Ag/AgCl with a scan rate of 5 mV s^{-1}. Tafel slopes can be obtained by plotting overpotential η against log (J) from LSV curves. A galvanostatic measurement at current density of 10 mA cm^{-2} was performed to test the stability of the catalyst. Accelerated degradation test was conducted for 1000 cyclic voltammetry (CV) cycles at scan rate of 50 mV s^{-1}. Electrochemical active surface areas (ECSAs) were measured by cyclic voltammetry (CV) at the potential window 0.2-0.3 V (vs. Ag/AgCl), with different scan rates of 20, 40, 60, 80, 100 and 120 mV s^{-1}. By plotting the $\Delta J = J_a - J_c$ at 0.25 V (vs. Ag/AgCl) against the

scan rate, the linear slope which is twice of the double layer capacitance (C_{dl}) is used to represent ECSAs. Electrochemical impedance spectroscopy (EIS) was measuring at overpotential bias of 300 mV from 0.1 to 10^5 Hz with an a.c. amplitude of 5 mV. Electrochemical data were corrected for the uncompensated series resistance R_s, which was determined through fitting of EIS data to a modified Randles circuit. The potential was determined by $E_{corrected} = E_{uncorrected} - iR_S$.

Turnover frequency

The TOF was calculated according to the following equation:

$$TOF = \frac{JA}{4Fm}$$

where J is the current density at a given overpotential, A is the surface area of the electrode (1.0 cm^2), F is Faraday constant (96,485 s A mol^{-1}) and m is the number of moles of the metal on the electrodes. In our cases, we assumed all the metal sites were actively involved in the electrochemical reaction.

Faradaic efficiency

The measurements of O_2 were performed in an air-tight H shape cell, which was divided by a glass frit to two chambers. The working electrode, the Ag/AgCl reference electrode and a magnetic stirring bar were inserted in one chamber of the cell, the Pt counter electrode was inserted in the other chamber. The cell was filled with 1.0 M KOH and degassed with argon for 2 h. The electrolysis was carried out with a constant oxidation current of 10 mA for 60 min. A measure of 500 μl of the gas sample in the compartment containing the working electrode was transferred by a specific syringe to the gas chromatography (Shimadzu) where the amount of O_2 evolution was determined. The Faradaic efficiency was determined from the total amount of charge Q (C) passed through the cell and the total amount of the produced O_2 n_{O2} (mol): $Faradaic\ efficiency = 4F \times n_{O_2}/Q$, where F is the Faraday constant, assuming the four electrons are needed to produce one oxygen molecule.

The ICP measurement details

1 cm^2 (1×1 cm) $FeVO_4$ electrode was cut out and dissolved into dilute HNO_3 solution (5 mL) with the help of ultrasound. Then, the sample solution was further diluted to 25 mL with deionized water, and measured with inductively coupled plasma optical emission spectrometry (ICP-MS, Agilent 725-ES).

Additional figures and discussions

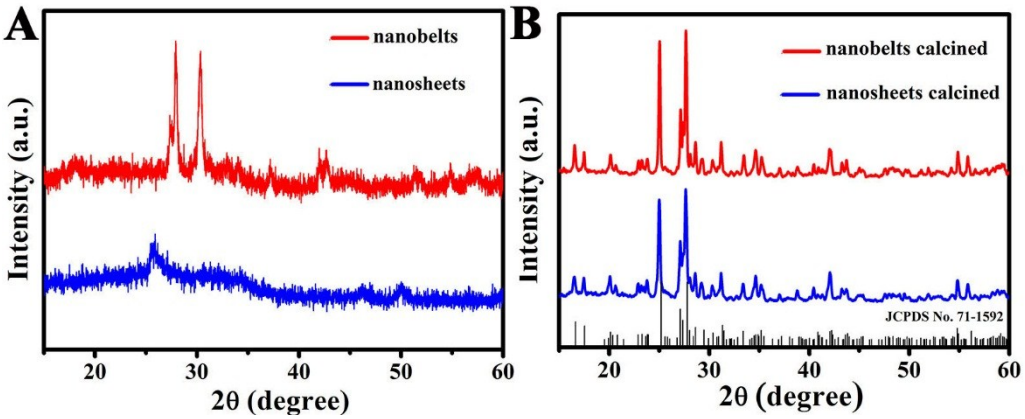

Fig. S1. XRD patterns of the $FeVO_4$ nanobelts and nanosheets (A) before and (B) after calcination at 550 ^oC for 2h. As shown in Fig. S1A, the as-prepared nanobelts and nanosheets were composed of hydrated iron-orthovanadates ($FeVO_4$), which could be assigned to $FeVO_4 \cdot 1.1H_2O$ based on previous structural studies[1, 2]. Owing to the hydrated functions, the crystallization degree of $FeVO_4$ was significantly decreased accompanied by evident changes on peak intensities and ratios in the XRD patterns[3]. Following dehydration process by the calcination treatments, the diffraction peaks of both nanobelts and nanosheets products (Fig. S1B) can be well indexed to the triclinic $FeVO_4$ (JCPDS No. 01-071-1592).

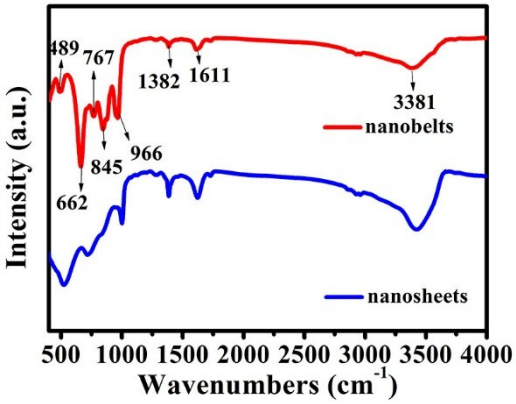

Fig. S2. FTIR patterns of nanobelts and nanosheets. The band at 3300 cm^{-1} clearly shows the presence of OH stretching of interlayer water molecules on the samples. The peak that emerges at 1611 cm^{-1} can be attributed to the bending vibration of interlayer H_2O. FTIR bands for all phases can be assigned to four major regions of $FeVO_4$, V-O terminal stretching (1050-850 cm^{-1}) and bridging V-O···Fe stretching (880-700 cm^{-1}), V···O···Fe stretching modes (700-550 cm^{-1}) and Fe-O stretching <550 cm^{-1}. Similarly, the peak intensity of the nanobelts become stronger compared with that of nanosheets, which is consistent with different morphologies and facets of nanobelts as observed by the XRD.

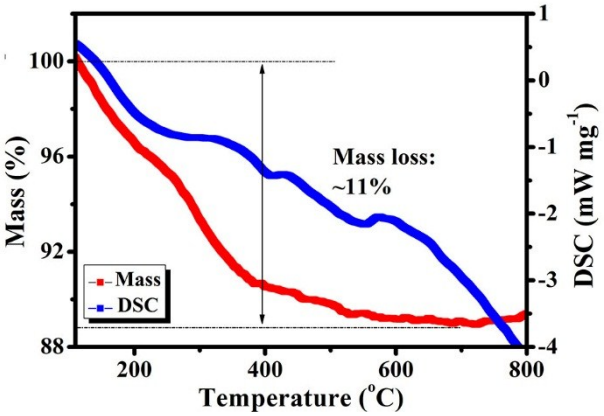

Fig. S3. TG/DSC curves of $FeVO_4$ nanobelts.

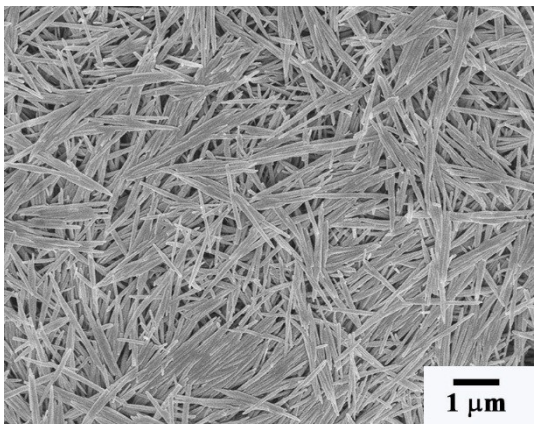

Fig. S4. SEM of $FeVO_4$ nanobelts.

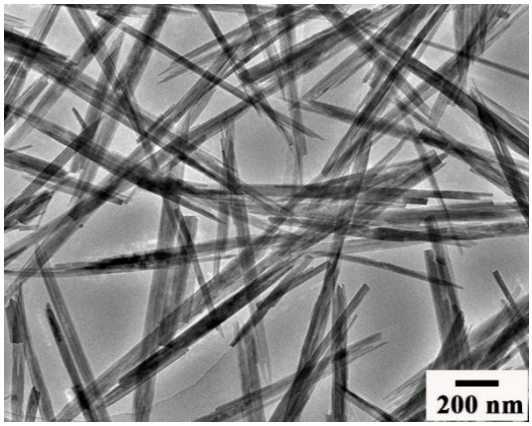

Fig. S5. TEM of $FeVO_4$ nanobelts.

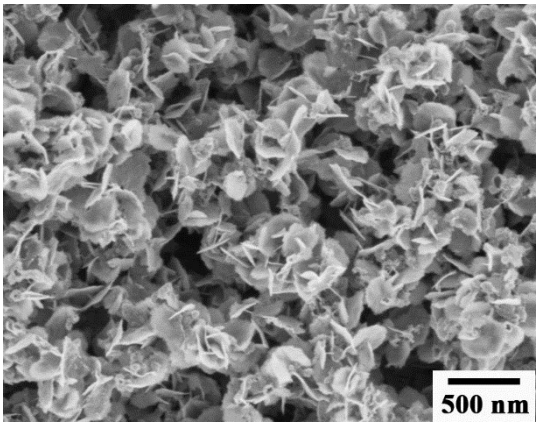

Fig. S6. SEM of $FeVO_4$ nanosheets.

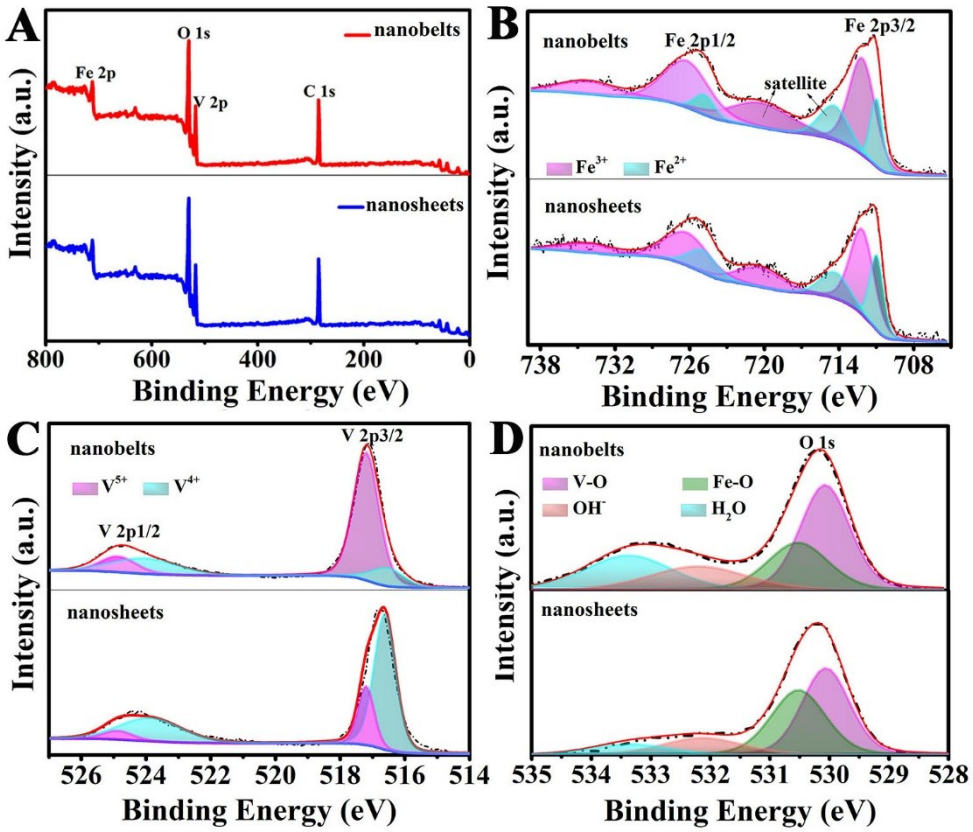

Fig. S7. XPS spectra of $FeVO_4$ crystals with different facets. (A) survey, and the core-level peaks of (B) Fe 2p, (C) V 2p and (D) O 1s.

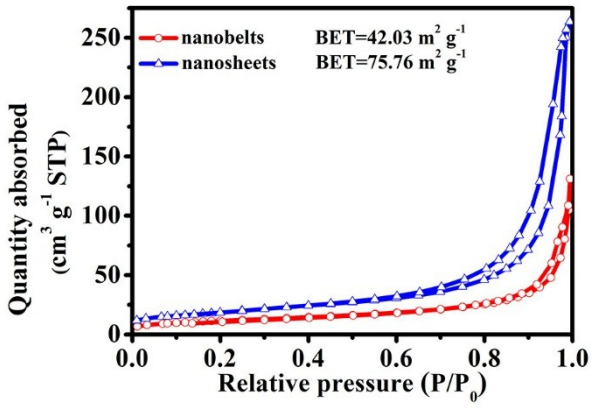

Fig. S8. N_2 adsorption-desorption isotherm of the as-prepared $FeVO_4$ catalysts.

Table S1. Comparison of the electrocatalytic OER activity of $FeVO_4$ nanobelts with {010} facets to other Fe-based and V based OER catalysts in 1.0 M KOH.

Electrocatalyst	***J* at η=300 mV (mA cm^{-2})**	**η at 10 mA cm^{-2} (mV)**	**Tafel slope (mV dec^{-1})**	**Ref.**
$FeVO_4$ nanobelts	90.7	240	37.39	This work
Fe-based thin film	~0	480	52	5
Fe-based film	~0	473	47	6
Amorphous FeOOH	~0	∽550	--	7
FeO_x	0.012 ± 0.007	405 ± 4	51 ± 3	8
$NiFeO_x$	~0	350	--	9
$CoFeO_x$	~0	380	--	9
$Fe_{0.5}V_{0.5}$ composite	~2.87	390	36.7	10
Fe_7S_8	~25	270	43	11
FeP_4 cubes	~76.33	260	41.4	12
$Fe(TCNQ)_2$ nanowire	~30.35	340	110	13
V nanobelts	~14.32	510	125	14
VOOH	~31.33	270	68	15
NiV LDH	~5.30	318	50	4
NiFe LDH	9.35	302	40	16
Rutile-RuO_2	~0.5	>470	--	17
Rutile-IrO_2	~0.76	>470	--	17

Table S2. Elemental analysis of nanobelts and nanosheets through ICP measurements.

Sample	Loading
nanobelts	0.66 mg cm^{-2}
nanosheets	0.67 mg cm^{-2}

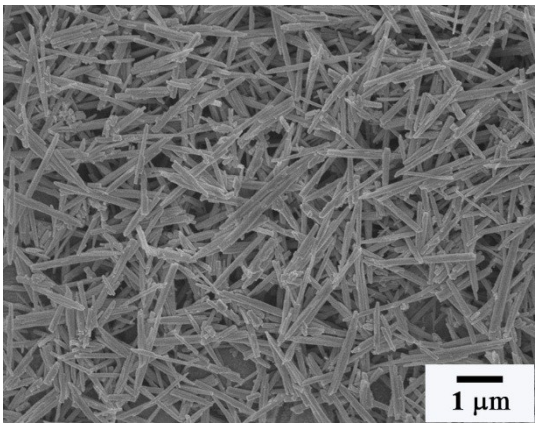

Fig. S9. SEM images of $FeVO_4$ nanobelts after OER. The morphology of the nanostructures of nanobelts had no obvious changes after the 1 h test.

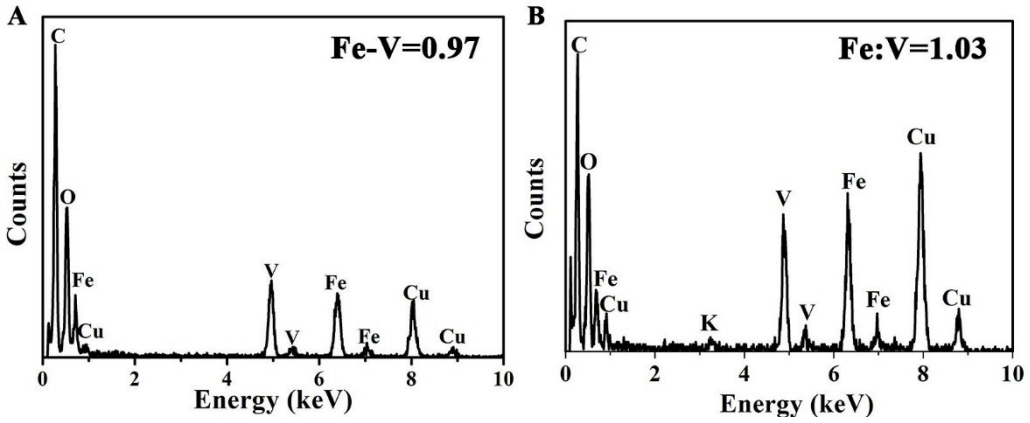

Fig. S10. EDS spectrum (C) before and (D) after OER. The Fe-V radio is nearly 1:1 before and after OER, indicating the bulk composition remains the same.

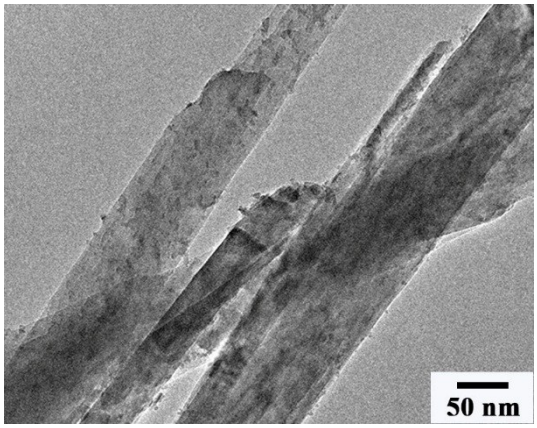

Fig. S11. TEM of $FeVO_4$ nanobelts after OER. After the OER, the TEM image reveals the surface of nanobelts become more roughness, and the EDX analysis shows the presence of K in the sample (Fig. S10B), which may be the KOH of the electrolyte on the surface of the nanobelts.

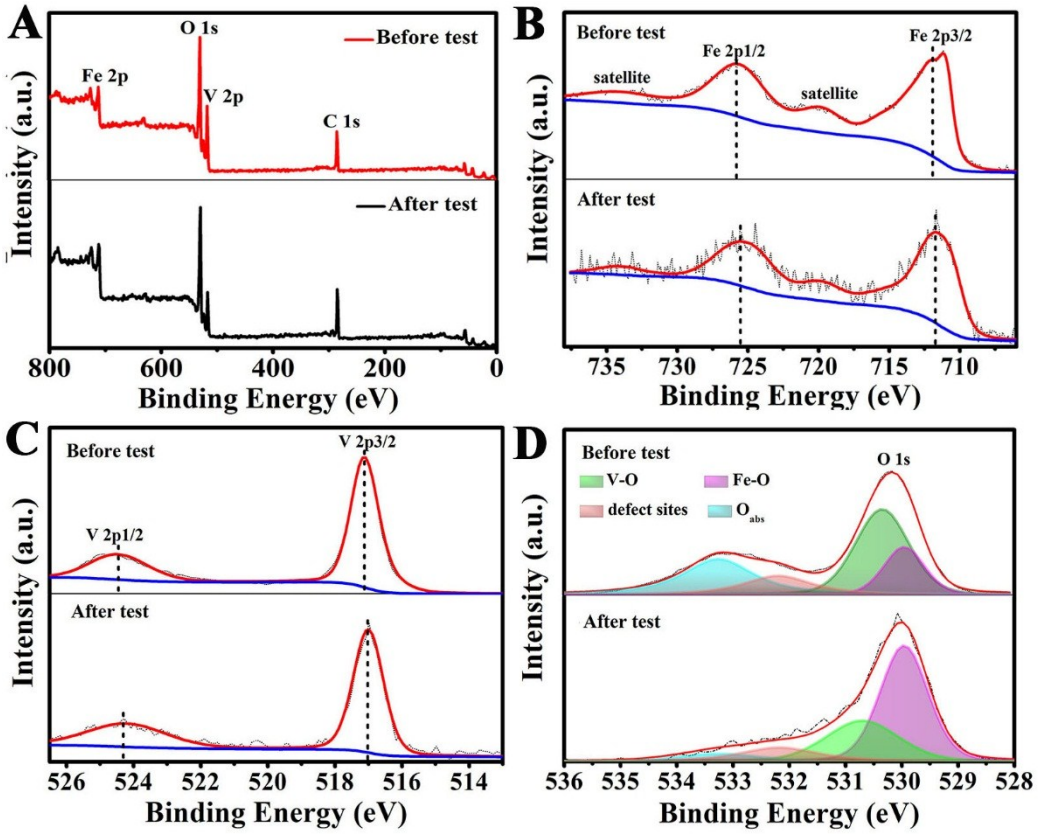

Fig. S12. XPS spectra of $FeVO_4$ nanobelts before and after OER: (A) survey, and the core-level peaks of (B) Fe 2p, (C) V 2p and (D) O 1s. No other elements or contaminants (except adventitious carbon) are detected in the survey spectrum after OER electrocatalysis, which confirm that nanobelts has a stable composition. After OER, the main peak positions from the Fe and V signals were nearly unchanged, which indicates the rapid generation of the new and stable surface species during catalysis[18, 19]. Meanwhile, the peak fitting analysis of O is changed, where the peak positions from H_2O and -OH signals are weakened (Fig. S12 D). This indicates that the surface oxidations happened on the active sites.

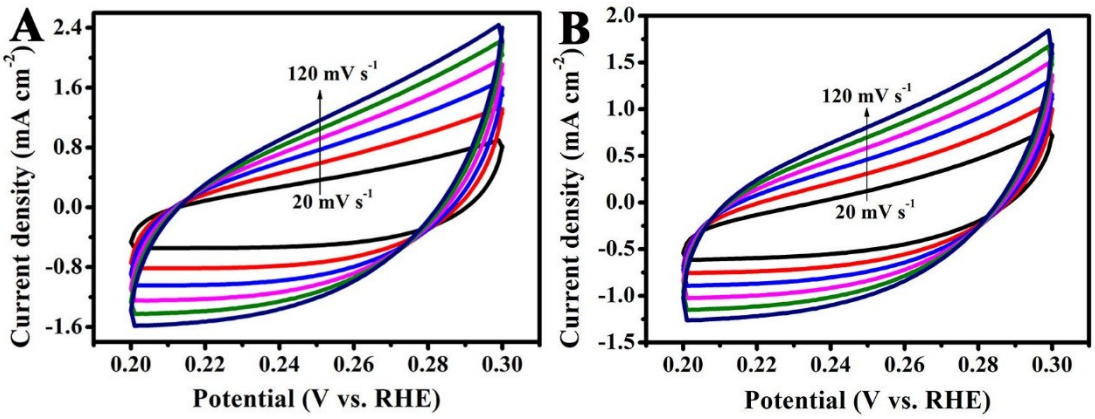

Fig. S13. Typical cyclic voltammograms recorded at different scan rates in the region of 1.20 V-1.30 V vs RHE upon OER catalysis for the determination of the double layer capacitance. (A) $FeVO_4$ nanobelts and (B) $FeVO_4$ nanosheets.

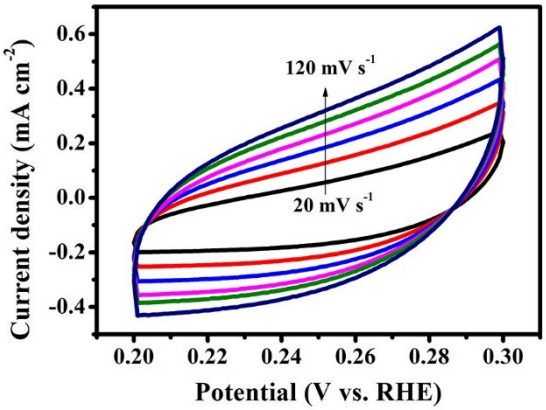

Fig. S14. Typical cyclic voltammograms recorded at different scan rates in the region of 1.20 V-1.30 V vs RHE upon bare NF for the determination of the double layer capacitance.

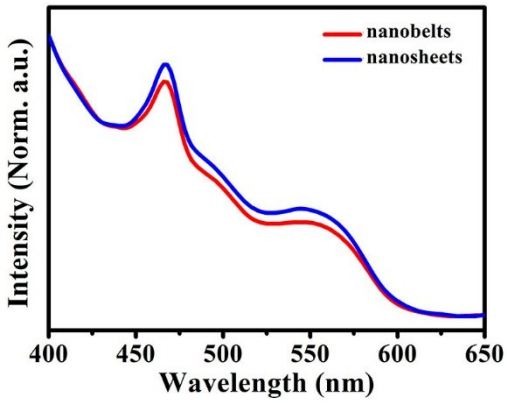

Fig. S15. Normalized PL spectra excited at 350 nm

Table S3. Fitting results of Nyquist plot in Fig. 3.

Samples	Rs(Ω)	CPE-T(F)	CPE-P(F)	Rct(Ω)

nanobelts	1.07	0.048	0.83	0.92
nanosheets	1.14	0.037	0.80	1.39

Table S4. Decay parameters of the two $FeVO_4$ nanocrystals.

Samples	Lifetime, (τ) (ns)	Pre-exponential factors B	Average Lifetime, (τ) (ns)[a]
nanobelts	τ_1=44.1	B_1=12.24	13.0
	τ_2=0.64	B_2=87.76	
nanosheets	τ_1=22.8	B_1=5.62	7.31
	τ_2=0.27	B_2=94.38	

[a] Average lifetime (τ) was determined according to the following equation [20]: $\tau = \frac{B_1T_1^2 + B_2T_2^2}{B_1T_1 + B_2T_2}$.

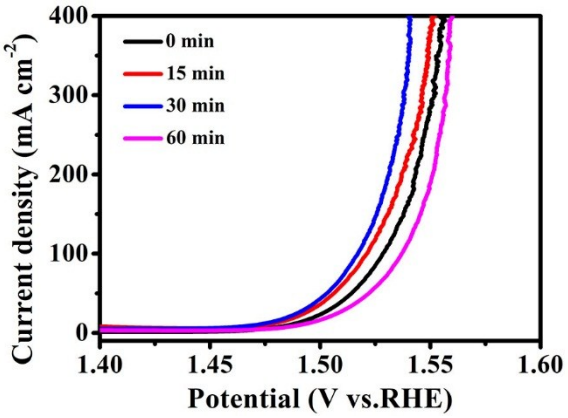

Fig. S16. The OER performance for $FeVO_4$ nanosheets treated in O_2-saturated 0.1 M VCl_3 for 0 min, 15 min, 30 min and 60 min, respectively. Notably, we can observe that the water oxidation activity of nanosheets increased with the treatment time less than 30 minutes, illustrating Fe sites on nanosheets {001} surfaces are preferably replaced by the added V sites. However, the over-treatment for 60 min can reduce the OER activity, because the excessive amounts of V ions inhibited its OER activities.

Additional discussion

The higher utilization of undersaturated Fe and V sites may play an important role in site

accessibility and catalysis of the OER. Bearing this in mind, the difference in the electrochemically active metal site density, which reflects the density of undercoordinated metal sites on the surface [21]. To eradicate the negative factors of Ni foam, the $FeVO_4$ catalyst was deposited on a pre-polished glassy carbon (GC) electrode with 3 mm diameter carefully (area: 0.07 cm^2) by the same method. The cathodic pseudocapacitive charge (q*cathodic) was carried out after performing OER in an Ar-saturated (Airgas, ultrahigh-grade purity) solution of 1.0 M KOH (Fig. S17 A) [21]. The charge density of the cathodic peak associated with the Fe (Ⅱ/Ⅲ) and V (Ⅳ/V) couples. Normalizing by the charge of two electron, the charge density for the nanobelts is similarly ~1.3 times higher than that of the nanosheets (Table S2). When the $FeVO_4$ films are polarized to more oxidative potentials in O_2-saturated electrolyte, the charge density at different facets are changed. Particularly, the charge density for the nanobelts surface is 4.4 nm^{-2}, which is higher than that on the nanosheets (4.1 nm^{-2}). This suggests a higher utilization of undersaturated Fe and V sites on the {010} faces at oxidizing potentials, which is active for the OER.

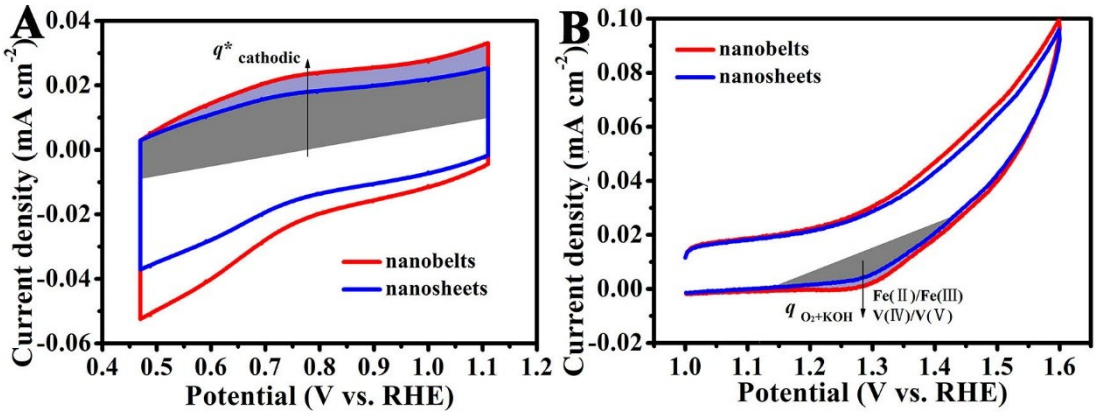

Fig.S17. (A) Charge passed from different $FeVO_4$ nanocrystals in Ar-saturated 1.0 M KOH at 50 mV s^{-1} as suggested by previous work to determine the charge density, q*cathodic[21]. (B) Anodic charge discernible from the double-layer capacitance from the Fe and V redox to determine of q_{O2+KOH}, in O_2-saturated 1.0 M KOH at 50 mV s^{-1}.

Table S5. Comparison of Charge Density from different $FeVO_4$ nanocrystals

Samples	$q^*_{cathodic}$ [μC cm^{-2}][a]	M_{q^*} density [nm^{-2}][b]	$q_{O_2+KOH}^*$ [μC cm^{-2}][c]	$M_{q_{O_2+KOH}^*}$ density [nm^{-2}][b]
nanobelts	349	10.9	141	4.4
nanosheets	272	8.5	132	4.1

[a] q^* cathodic was measured in Ar-saturated KOH and includes double-layer capacitance. [b] M_{q^*} density is the associated electron density from q^* cathodic, assuming 2 e$^-$ transfer. [c] $q_{O_2+KOH}^*$ is anodic charge discernible from the double-layer capacitance.

Additional discussion

The surface adsorbed oxygen on the {010} surfaces can affect the catalytic activity [22]. Meanwhile, investigating XPS again, the nanobelts with {010} facets owned the most abundant O_{ads}, which tends to participate into the oxidation reaction[22]. H_2-TPR experiments were performed to investigate the reducibility of the samples and distinguish the catalytic activity of surface adsorbed oxygen. As shown in Fig. S18, the temperatures corresponding to the reduction process followed the order nanobelts {010} < nanosheets {001}. The nanobelts with {010} faces show a reduction peak at the lowest temperature, indicating the most mobile oxygen species both at the surface and in the bulk [23, 24]. Accordingly, the high oxygen mobility causes more active intermediate to be adsorbed and further excited to active oxygen. In addition, the contact angles results indicated the advantageous hydrophilic ability of the nanobelts (Fig. S19). Because of its higher-water content and better water adsorption ability, nanobelts with {010} facets showed excellent activity for OER.

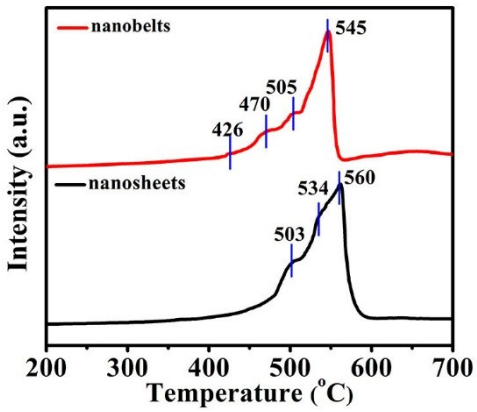

Fig. S18. H_2-TPR of nanobelts and nanosheets. H_2-TPR experiments were performed to investigate the reducibility of the samples and distinguish the catalytic activity of surface adsorbed oxygen.

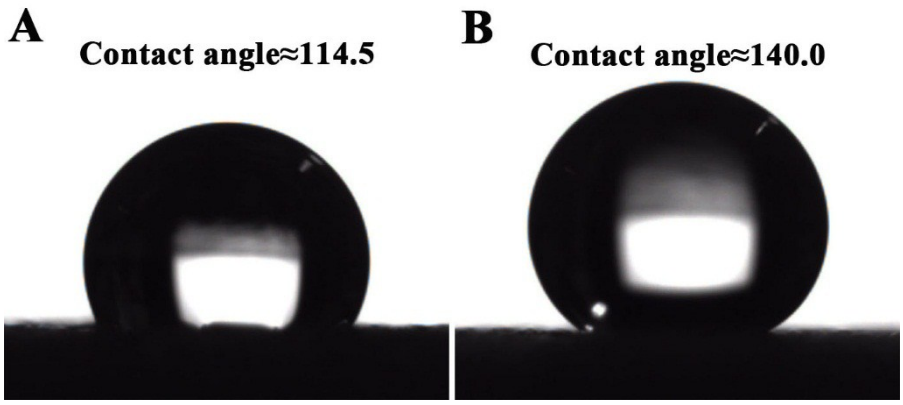

Fig. S19. Contact angle of (A) nanobelts and (B) nanosheets.

Additional discussion

Inspired by the good OER activity, we then assembled Faradaic efficiency and overall water splitting of $FeVO_4$ nanobelts with {010} facets. The experimental and theoretical O_2 evolution amount of {010} facets were performed at a current density of 10 mA cm^{-2} in 1.0 mol L^{-1} KOH (Fig. S20). The O_2 evolution of {010} facet electrocatalyst was measured by a gas chromatography with the electrolysis time of 60 min. Comparing the experimental data with the theoretical data, the amount of oxygen evolved corresponds to a Faradaic yield of >95%, as shown in Fig. S20. What's more, to further explore the highly water splitting activity of {010} facet, as shown in Fig. S21 A, we then assembled a full electrochemical cell using the $FeVO_4$ nanobelts as anode and platinum cathode for overall water splitting. The same measurement was also

conducted for nanosheets for comparison. The nanobelts can deliver a current density of 10 mA cm^{-2} at 1. 63 V, which is lower than that of nanosheets (1.79 V). This result indicates attractive prospects for using $FeVO_4$ nanobelts in operational water electrolysis systems.

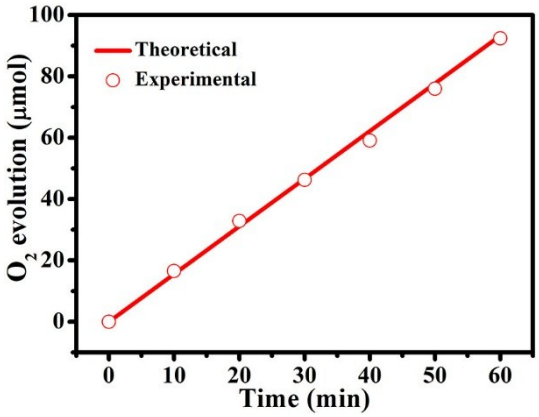

Fig. S20. (A) Oxygen efficiency of nanobelts under a fixed current density of 10 mA cm^{-2} in 1.0 mol L^{-1} KOH.

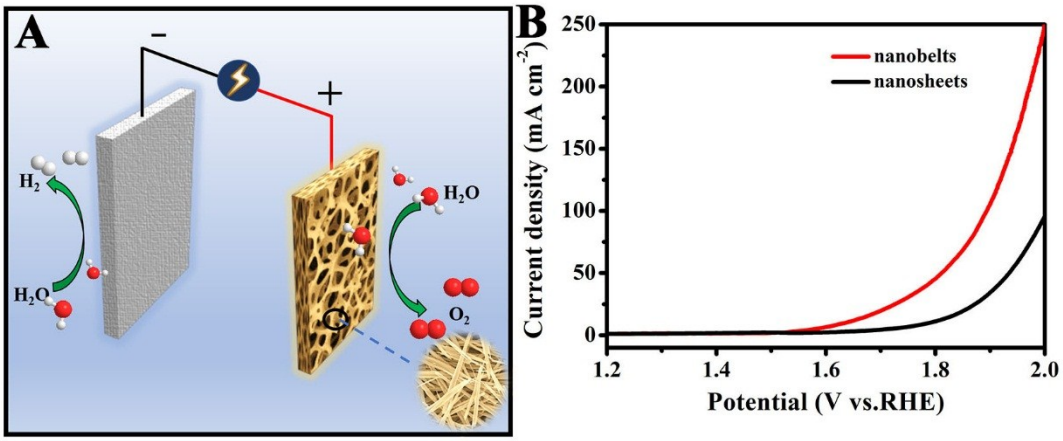

Fig. S21. (A) schematic illustration of a two-electrode cell for overall water splitting, which $FeVO_4$ nanobelts or nanosheets used an anode and platinum a cathode. (B) Polarization curve of overall water splitting.

References

1 Y. V. Kaneti, Z. J. Zhang, J. Yue, X. C. Jiang, A. B. Yu, *J Nanopart Res,* 2013, **15**, 1948.

2 P. Poizot, E. Baudrin, S. Laruelle, L. Dupont, M. Touboul, J. M. Tarascon, *Solid State Ionics,* 2000, **138**, 31-40.

3 A. Š. Vuk, B. Orel, G. Dražič, F. Decker, P. Colomban, *J Sol-Gel Sci Techn*, **23**, 165-181.

4 K. Fan, H. Chen, Y. Ji, H. Huang, P. M. Claesson, Q. Daniel, B. Philippe, H. Rensmo, F. Li, Y. Luo and L. Sun, *Nat Commun*, 2016, **7**, 11981.

5 Y. Wu, M. Chen, Y. Han, H. Luo, X. Su, M. T. Zhang, X. Lin, J. Sun, L. Wang, L. Deng, W. Zhang, R. Cao, *Angew Chem Int Ed,* 2015, **54**, 4870-4875.

6 M. Chen, Y. Wu, Y. Han, X. Lin, J. Sun, W. Zhang, R. Cao, *ACS Appl Mater Inter*, 2015, **7**,

21852-21859.
7 W. D. Chemelewski, H. C. Lee, J. F. Lin, A. J. Bard, C. B. Mullins, *J Am Chem Soc*, 2014, **136**, 2843-2850.
8 L. Trotochaud, J. K. Ranney, K. N. Williams, S. W. Boettcher, *J Am Chem Soc*, 2012, **134**, 17253-17261.
9 C. C. L. McCrory, S. Jung, J. C. Peters, T. F. Jaramillo, *J Am Chem Soc*, 2013, **135**, 16977-16987.
10 K. Fan, Y. Ji, H. Zou, J. Zhang, B. Zhu, H. Chen, Q. Daniel, Y. Luo, J. Yu, L. Sun, *Angew Chem Int Ed*, 2017, **56**, 3289-3293.
11 S. Chen, Z. Kang, X. Zhang, J. Xie, H. Wang, W. Shao, X. Zheng, W. Yan, B. Pan, Y. Xie, *ACS Cent Sci*, 2017, **3**, 1221-1227.
12 Q. He, H. Xie, Z. u. Rehman, C. Wang, P. Wan, H. Jiang, W. Chu, L. Song, *ACS Energy Lett*, 2018, **3**, 861-868.
13 M. Xie, X. Xiong, L. Yang, X. Shi, A. M. Asiri, X. Sun, Chem. Commun. 2018, **54**, 2300-2303.
14 Y. Yu, P. Li, X. Wang, W. Gao, Z. Shen, Y. Zhu, S. Yang, W. Song, K. Ding, *Nanoscale* 2016, **8**, 10731-10738.
15 H. Shi, H. Liang, F. Ming, Z. Wang, Angew. Chem. Int. Ed.l 2017, **56**, 573-577.
16 F. Song, X. Hu, *Nat Commun*, 2014, **5**, 4477.
17 Y. Lee, J. Suntivich, K. J. May, E. E. Perry, Y. Shao-Horn, *J Phys Chem Lett*, 2012, 3, 399-404.
18 S. Wan, J. Qi, W. Zhang, W. Wang, S. Zhang, K. Liu, H. Zheng, J. Sun, S. Wang, R. Cao, *Adv Mater*, 2017, **29**, 1700286.
19 Y. Yang, L. Dang, M. J. Shearer, H. Sheng, W. Li, J. Chen, P. Xiao, Y. Zhang, R. J. Hamers and S. Jin, *Adv Energy Mater*, 2018, 1703189.
20 W. Zhen, J. Ma, G. Lu, *Appl Catal B*, 2016, **190**, 12-25.
21 K. A. Stoerzinger, L. Qiao, M. D. Biegalski, Y. Shao-Horn, *J Phys Chem Lett*, 2014, **5**, 1636-1641.
22 J. Chen, A. Selloni, *J Phys Chem Lett*, 2012, **3**, 2808-2814.
23 S. Rong, P. Zhang, F. Liu, Y. Yang, *ACS Catal*, 2018, **8**, 3435-3446.
24 M. Knapp, A. P. Seitsonen, Y. D. Kim, H. Over, *J Phys Chem B*, 2004, **108**, 14392-14397.